Chinese Journal of Mechanical Engineering

ORIGINAL ARTICLE

Open Access

Surface Integrity of Inconel 738LC Parts Manufactured by Selective Laser Melting Followed by High-speed Milling

Guanhui Ren[1,2,3,4], Sai Guo[1,2] and Bi Zhang[1,2*]

Abstract

This study is concerned with the surface integrity of Inconel 738LC parts manufactured by selective laser melting (SLM) followed by high-speed milling (HSM). In the investigation process of surface integrity, the study employs ultra-depth three-dimensional microscopy, laser scanning confocal microscopy, scanning electron microscopy, electron backscatter diffractometry, and energy dispersive spectroscopy to characterize the evolution of material microstructure, work hardening, residual stress coupling, and anisotropic effect of the building direction on surface integrity of the samples. The results show that SLM/HSM hybrid manufacturing can be an effective method to obtain better surface quality with a thinner machining metamorphic layer. High-speed machining is adopted to reduce cutting force and suppress machining heat, which is an effective way to produce better surface mechanical properties during the SLM/HSM hybrid manufacturing process. In general, high-speed milling of the SLM-built Inconel 738LC samples offers better surface integrity, compared to simplex additive manufacturing or casting.

Keywords Surface integrity, Inconel 738LC, Selective laser melting, High-speed milling

1 Introduction

Inconel 738LC is a face-centered cubic (FCC) structural and γ′ phase precipitation hardening nickel-based superalloy with high temperature strength, toughness, hardness, and wear resistance, and has been widely used in the shipbuilding, chemical, and petrochemical industries. It can be also applied to aerospace engines and supersonic aircraft [1]. However, Inconel 738LC is a representative of difficult-to-machine material on account of its low thermal conductivity and high reactivity with milling tools [2]. For Inconel 738LC or other difficult-to-machine materials, selective laser melting (SLM) technology shows unique advantages as a newly emerging manufacturing technology. It integrates computer-aided design (CAD), material processing and forming technologies by using software and numerical control systems to melt and solidify materials layer by layer to manufacture complex structural parts with high integration and multifunction. SLM makes it easier to manufacture parts that are otherwise constrained by the machining processes in conventional subtractive manufacturing. Moreover, SLM greatly simplifies design and speeds up the product development cycle [3, 4]. Nevertheless, SLM adopts a two-dimensional layering method in the discretization process, which always results in size errors and defects. Therefore, the mechanical properties and surface integrity of SLMed Inconel 738LC parts are generally poor, which substantially impedes its practical applications [5, 6].

*Correspondence:
Bi Zhang
zhangb@sustech.edu.cn
[1] Department of Mechanical and Energy Engineering, Southern University of Science and Technology, Shenzhen 518055, China
[2] Shenzhen Key Laboratory for Additive Manufacturing of High-performance Materials, Shenzhen 518055, China
[3] Research and Development Department, Shenzhen Xinjinquan Precision Techonology Co., Ltd., Shenzhen 518055, China
[4] School of Mechanical Engineering, Shandong University, Jinan 250061, China

In order to ameliorate the inferior mechanical properties and surface integrity of SLMed Inconel 738LC parts, Du et al. [7] employed a novel technical route named SLM/high-speed milling (HSM) hybrid manufacturing, i.e., additive/subtractive hybrid manufacturing (ASHM). For parts with complex geometric structures or difficult-to-machine materials, the near-net shape process can be completed by additive manufacturing, the subsequent finishing can be completed by subtractive manufacturing. As illustrated in Figure 1, a hybrid manufacturing system may at least consists of a multi-axis machining center and material deposition system. The key technologies include optimization of ASHM, construction of software and hardware platforms, and development of a control system. In the hybrid manufacturing process, since SLM and HSM are conducted alternately, geometric error compensation and material removal schemes should be reserved and determined at the CAD model design phase. Subsequently, a three-dimensional CAD model in STL format is sliced into layers by slicing software. Based on a two-dimensional discrete file, laser scanning paths are planned by the additive process control unit. Meanwhile, HSM paths are planned by the subtractive process control unit. After a fiber laser beam scans and melts the metal powders for every 10–15 layers, HSM is performed subsequently. The hybrid manufacturing process is conducted alternately until the whole part is finished, as illustrated in Figure 2 [8]. Because the addition, subtraction, and inspection processes are completed in a single machine system, it not only suppresses the errors caused by re-positioning the part in multi-platform manufacturing, improves manufacturing accuracy and production efficiency, but also saves space and reduces manufacturing costs.

ASHM has been paid more and more attention in both the academic and industrial sectors in recent years. Sunshine Laser & Electronics [8] and Sodick [9] independently developed SLM/HSM hybrid machine tools and overcame key technological challenges, such as the adaption of a laser scanning system to avoid structural interferences between SLM and HSM system, the process planning and data processing system to coordinate

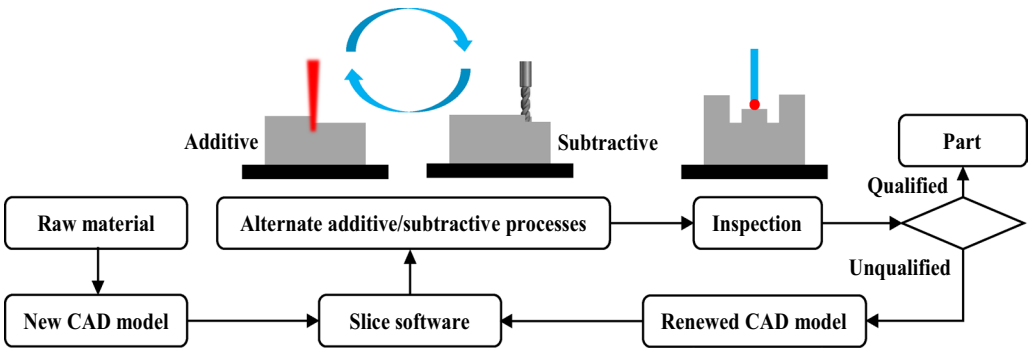

Figure 1 SLM/HSM hybrid manufacturing system

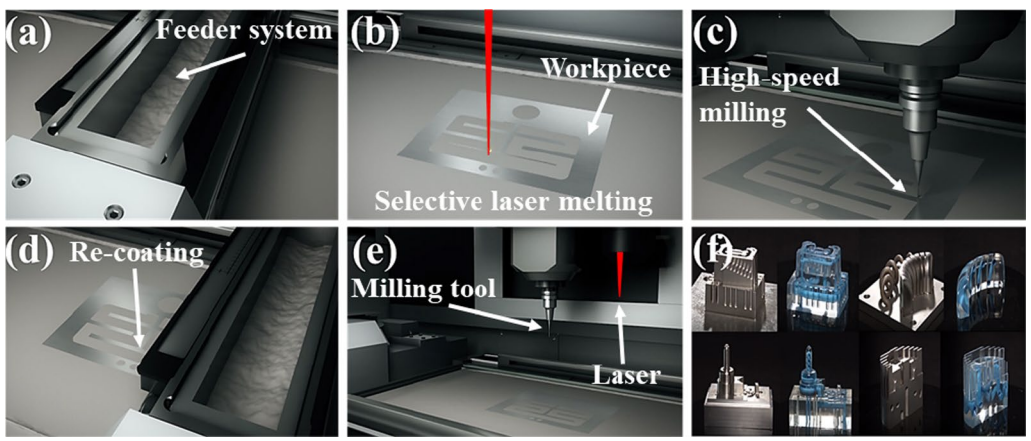

Figure 2 SLM/HSM hybrid manufacturing process [14]: **a** Feeder system; **b** Selective laser melting process; **c** High-speed milling process; **d** Re-coating; **e** SLM/HSM hybrid manufacturing; **f** Sample parts with complex inner passages and external profiles

Table 1 Chemical compositions of the Inconel 738LC powders.

Element	Content (wt.%)	Element	Content (wt.%)	Element	Content (wt.%)
Cr	15.82	Al	3.48	N	0.005
Co	8.32	Ti	0.12	B	0.01
W	2.58	C	0.88	Zr	0.058
Mo	1.82	Nb	1.78	Ni	Balance
Ta	3.5	O	0.0154		

Table 2 Chemical compositions of the milling tool material

Element	Ti	W	Co	C	Ta
Content (wt.%)	4.8	77.0	8.0	6.45	3.75

SLM/HSM. Wang et al. [10] investigated the influence of a protective atmosphere on the mechanical properties and microstructures of the commercial pure Ti and conferred superb strength to commercial pure Ti without sacrificing its ductility through SLM by using a high-power laser and incorporating solute atoms from the Ar-N_2 reactive atmosphere. Du et al. [11] performed an ASHM experiment on 18Ni-300 steel, and found different microstructures and residual stress evolutions of a hybrid-manufactured part from that of the traditional mechanical manufacturing processes. Debajyoti et al. [12] investigated surface/interface quality, microstructure and mechanical properties of ASHMed parts, and found that the ultimate tensile strength (UTS) of the hybrid manufacturing bars was higher than those of the heat-treated bars. Bai et al. [13] conducted a hybrid manufacturing experimental study on the manufacturing of a 6511 martensitic stainless steel and found that the surface residual stress state and distribution could be controlled in the milling process.

Although some research on ASHM process and equipment have been reported, no research on surface integrity is found. Therefore, this study investigates the surface integrity of high-speed milling of SLM-built Inconel 738LC parts in regard to powder morphology, surface quality, microstructure alteration, and mechanical property.

2 Experimental Procedure

2.1 Experimental Material

The experimental material was Inconel 738LC powder (GBT14992-2005, AMC POWDERS Ltd., China). Its morphology and particle size were observed with a scanning electron microscope (SEM, TM4000-Plus, Hitachi, Japan) and measured by a particle size analyzer (Mastersizer 3000, Malvern, UK). Its chemical compositions were analyzed by an energy dispersive spectrometer (EDS, Octane Pro, EDAX, England), and the result is illustrated in Table 1. Table 2 shows the chemical compositions of the end milling tools made of solid carbides (EMTC4S-D8-20, CASIC Tools Ltd., China) used in the experiment. Shielding Ar with a purity of 99.9 vol. % was supplied during the manufacturing process. In addition, the as-cast Inconel 738LC alloy samples were used in the experiment for comparison.

2.2 Additive and Subtractive Manufacturing Processes

As illustrated in Figure 3, a three-dimensional CAD model in STL format was sliced into layers by slicing software first. Then, an orthogonal scanning strategy was adopted to reduce the deformation caused by residual stresses. In this strategy, the *XY* surface was perpendicular to the building direction, while the *YZ* and *ZX* surfaces were parallel to the building direction. Volume

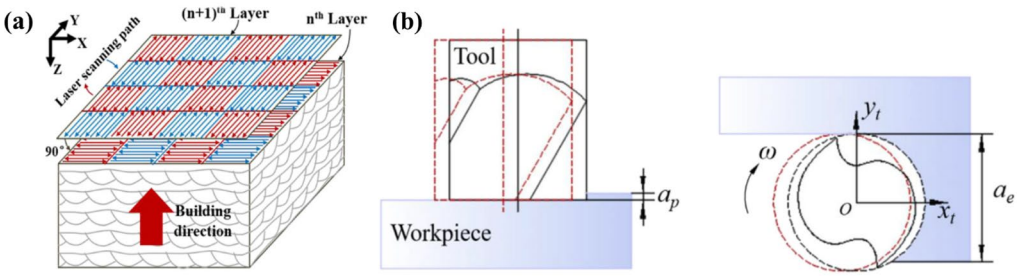

Figure 3 Schematics of **a** the scanning strategy for SLM and **b** for HSM [13]

energy density (VED) usually plays a decisive role in determining the material quality and is used to guide the selection of the appropriate SLM processing parameters, such as laser power, scan speed, hatch spacing, and layer thickness,

$$VED = \frac{P}{v \cdot h \cdot t}, \quad (1)$$

where P is laser power; v is laser scanning speed; h is hatch distance; and t is layer thickness.

After the substrate is covered with the Inconel 738LC powders, a fiber laser subsequently scans across and melts the powders. After one layer is scanned, the platform descends one layer. Then, the powder is spread for another layer, and the laser scanning is applied again. After the powder-spreading and laser-scanning processes are repeated for 10–15 layers, HSM begins. The additive and subtractive processes are executed until the Inconel 738LC sample is finished. According to the ISO 13399 standard, the fiber laser/milling tool and process parameters are presented in Table 3.

2.3 Surface Integrity Characterization

A laser scanning confocal microscope (VK-X1000, KEYENCE, Japan) was used to measure surface morphology and roughness of the samples. A precision slow-feeding NC wire-cut machine (AG400L, Sodick, Japan) was used to cut the samples. A lapping and polishing machine (MP-1B, WeiYi, China) was used to buff the metallographic samples. A digital display microhardness tester (HVS-1000-PC, China) was used to measure Vickers microhardness of the metallographic samples with a 0.49 N load holding for 10 s for each measurement. A Kalling's 2 corrosive liquid was used to etch the metallographic samples. A digital microscope (VHX-7000, KEYENCE, Japan) was used to observe the metallographic microstructures. The samples for electron backscatter diffraction (EBSD) observations were further polished by a vibratory polisher (VibroMet® 2, Buehler, USA), and observed in an SEM (Zeiss Merlin, Germany) equipped with an EBSD Camera (Velocity™, AMETEK, USA). An EDAX® TSL™ OIM analysis software was used to estimate the EBSD data. An X-ray residual stress analyzing facility (μ-X360s, Pulstec, Japan) was used to measure residual stresses of the SLMed and SLMed/HSMed samples.

3 Results

3.1 Effect of Material Powders

As illustrated in Figure 4, the Inconel 738LC had several different morphologies of powders, such as nearly spherical, peanut shaped, and rod-shaped. The size distribution of the Inconel 738LC powders is illustrated in Figure 4g. It can be seen from the curve that the sampling data has a close-to-normal distribution with the powder size in the range of 18.8–67.2 μm. The larger powders were attached with many satellite powders and burrs, while the smaller powders showed relatively smooth surfaces [15]. Size grading D_v (10), D_v (50) and D_v (90) are 18.8 μm, 33.0 μm and 67.2 μm, respectively.

The details on the role of the powder size in surface defects and roughness have been reported elsewhere [16]. The particle size of the powders has a significant effect on surface defects and roughness. Generally, the larger the powder size, the larger the surface roughness [17]. The rough surface changes the incident angle of the laser beam, so that the laser beam is reflected many times, and its energy is absorbed repeatedly. The larger the powder size, the higher the laser absorption rate [18]. When the powder size is too large, the thickness and uniformity of the powder layer are difficult to control, which may in turn affect the stability of laser scanning [19]. As illustrated in Figures 5 and 6, the height and width variations of the cladding humps varied with powder size and shape, which explains the topographic formation mechanism of the adjacent cladding in the same layer. In addition, the

Table 3 Fiber laser/milling tool and process parameters

Fiber laser/milling tool parameters	Quantitative value	Process parameters	Quantitative value
Maximum laser output (W)	500	Laser power (W)	270
Laser wavelength (nm)	1070	Scanning speed (mm/s)	950
Laser spot size (μm)	90	Layer thickness (μm)	30
Cutting diameter (mm)	8	Hatch spacing (μm)	90
Connection diameter (mm)	8	Spindle speed n (r/min)	5000
Functional length (mm)	60	Cutting velocity v (m/min)	126
Maximum cutting depth (mm)	19	Feed rate f (mm/min)	50
Number of tool tooth	4	Cutting depth a_p (mm)	1
Peripheral effective cutting length (mm)	6	Cutting width a_e (mm)	0.2

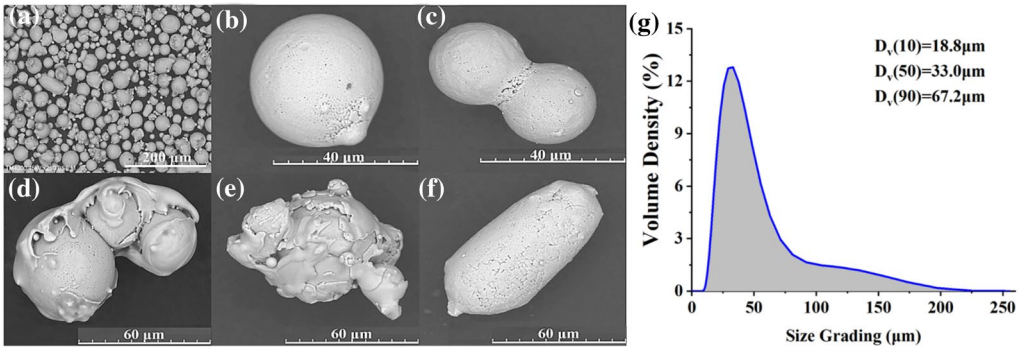

Figure 4 **a** Inconel 738LC powders; **b** A near spherically shaped powder; **c** A peanut-shaped powder; **d**, **e** Irregular shape powders; **f** A rod-shaped powder; **g** Powder size grading

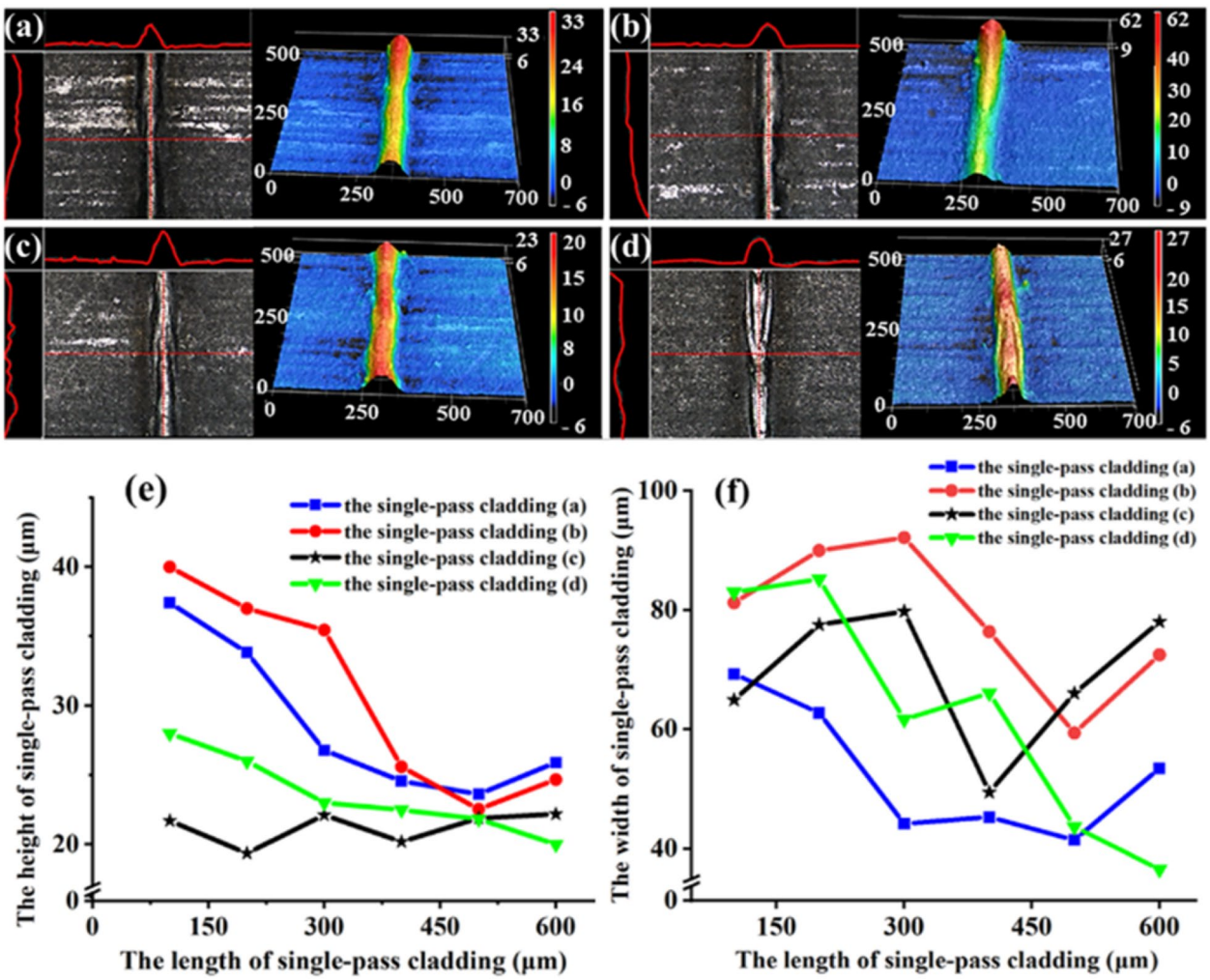

Figure 5 **a**–**d** Different single-pass claddings; **e** The height variation of single-pass claddings; **f** The width variation of single-pass claddings

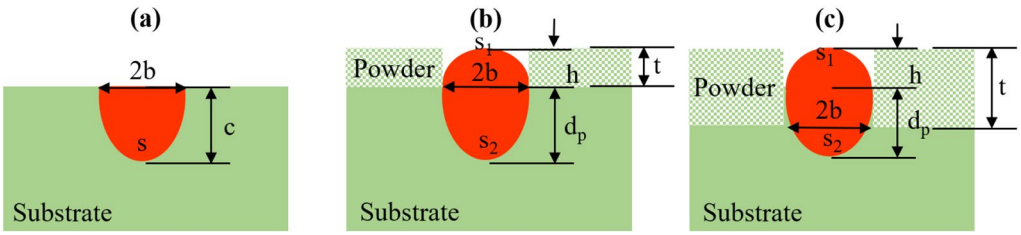

Figure 6 Schematics of single-pass cladding cross-sections: **a** The bare substrate without powder; **b** The first powder layer; **c** The *k*th powder layer ($k>7$)

powders with irregular shapes often have internal pores which may contribute to defect formation due to the internal pores dragging into the melt pool. Moreover, it is well known that the formation of pore defects in additive manufacturing process is closely related to the "keyhole effect" which is formed by the vaporization of the molten pool materials under the recoil pressure of the laser [20, 21].

For simplification, the keyhole is assumed to be a half ellipse, its cross-section area $S=\pi bc/2$ and width $2b$ are assumed to be independent of the powder layer thickness as illustrated in Figure 6(a). Based on the model, the powder layer thickness of the first layer is t, and because the powders are near-sphere, the powder packing density of the first layer is illustrated in Figure 6(b). Based on the mass conservation, the area of hump S_1 is roughly equivalent to the actual area of the original Inconel 738LC powders, and the depth of keyhole d_p is evaluated from the area of keyhole S_2 [22]:

$$\text{Hump area} \quad S_1 = 2bt, \tag{2}$$

$$\text{Keyhole area} \quad S_2 = S - S_1, \tag{3}$$

$$\text{Keyhole depth} \quad d_p = \frac{2S_2}{\pi b} = c - 4\pi t. \tag{4}$$

From Eqs. (2)–(4) [23], the powder layer thickness has a conspicuous effect on the keyhole depth for the k^{th} layer. Therefore, keyhole depth d_p needs to be considered when evaluating surface integrity, where the uppermost k^{th} powder layer ($k>7$) plays an important role. The powder size distribution is one of the most important factors for the apparent density of powder layer. The narrower the powder size distribution range, the higher the apparent density of the powder layer [24]. In theory, smaller particle size is beneficial to obtaining a higher apparent density of the powder layer, so as to further obtain parts with higher volume density. However, the agglomeration tendency of the small powders significantly restricts the flowability of the powders [25]. Although large size powders can significantly restrain the agglomeration tendency, they can also reduce the apparent density of the powder layer, leading to lower volume density. Consequently, it is necessary to consider the role of Inconel 738LC alloy powder size so as to select an optimized powder size for better surface integrity of a fabricated part.

3.2 Effect of Processing Strategy

A remarkable correlation of surface morphology with building direction during the SLM process can be seen in Figure 7(a)–(c). The SLMed sample showed different surface morphologies in different directions, which is strikingly different from the surface of as-cast sample as illustrated in Figure 7(d). The *XY* surface indicates the smallest *Ra* 0.77 and *Sa* 1.4, which is significantly better than as-cast sample as illustrated in Figure 9(a). In addition, as illustrated in Figures 3 and 8, the surface morphologies and roughness of the SLMed samples were greatly affected by the scanning strategy and the processing parameters. For different scanning strategies and parameters, completely different surface morphologies and roughness were obtained. On the same layer, a part of the previous single-pass cladding was remelted in the scanning direction. Between the adjacent claddings on the same layer, remelting region between the adjacent claddings is determined by a proportional relationship between the scanning distance and the width of the cladding, as illustrated in Figure 7(a). Between the adjacent layers, the previous layer is remelted to firmly join with the adjacent layers. The hump is from the melted Inconel 738LC powders on account of fluid surface tension, as illustrated in Figure 7(b) and (c).

In the manufacturing process, since SLM and HSM were conducted alternately, material forming error compensation and removal amount during the HSM process should be reserved and determined according to the surface quality and morphologies generated in the SLM process. A remarkable difference in the surface morphologies between the samples made by different processes

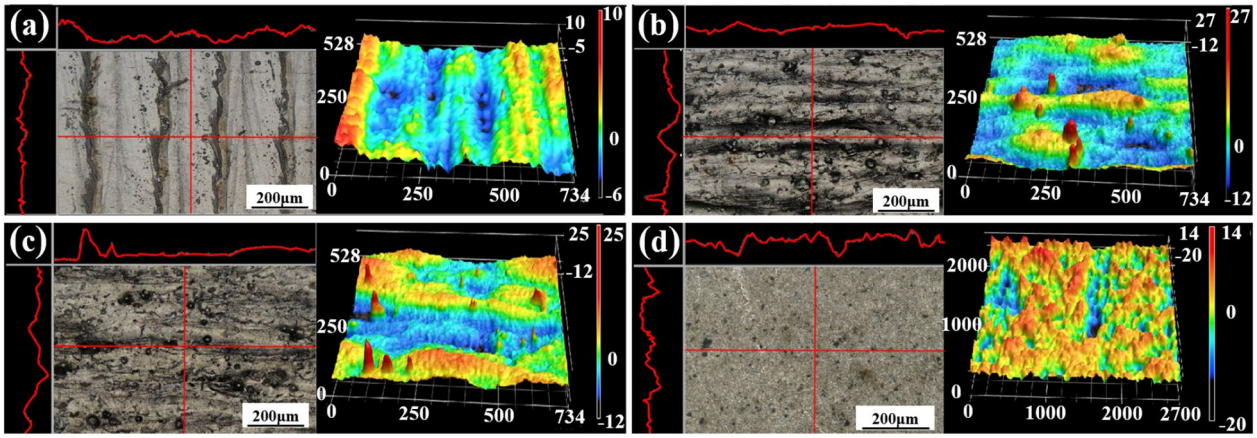

Figure 7 **a**–**c** Surface morphology and 3D display of the *XY*, *YZ* and *ZX* surface of the SLMed sample; **d** Surface morphology and 3D display of the as-cast sample

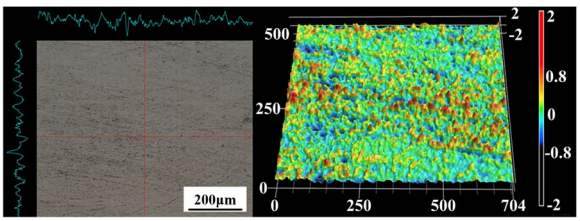

Figure 8 Surface morphology and 3D display of the SLMed/HSMed samples

can be seen in Figures 7, 8 and 9. Surface roughness of the SLMed/HSMed sample diminished at least one order of magnitude compared to that of the SLMed sample. *Ra* of the SLMed/HSMed sample was in a range of 0.15–0.2 μm. Compared to parts manufactured by the simplex SLM or casting, the SLMed/HSMed parts demonstrated much better surface roughness.

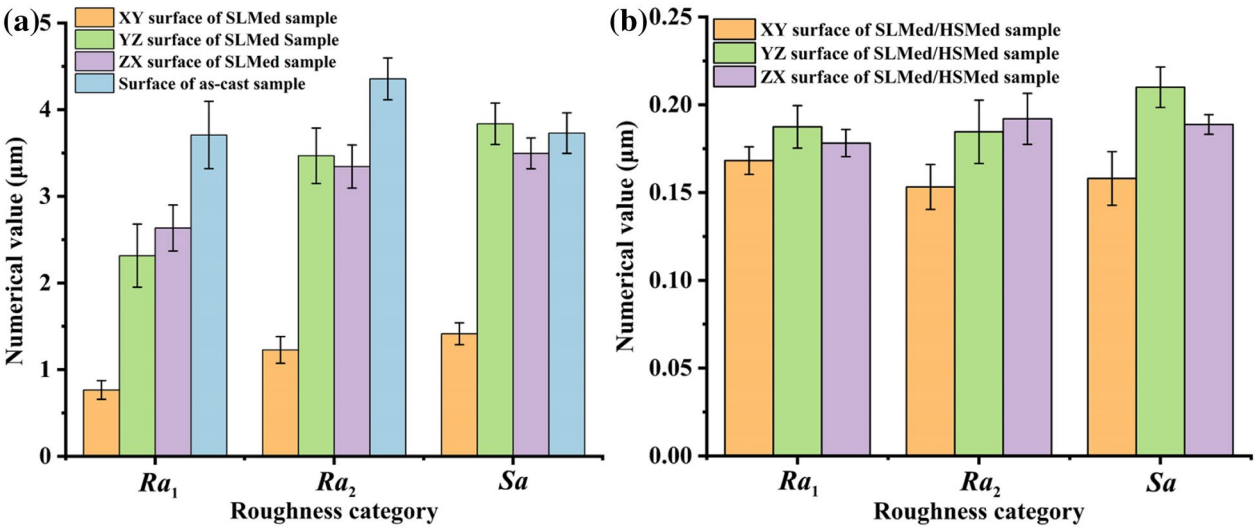

Figure 9 Surface roughness of **a** the SLMed and as-cast samples; **b** SLMed/HSMed samples

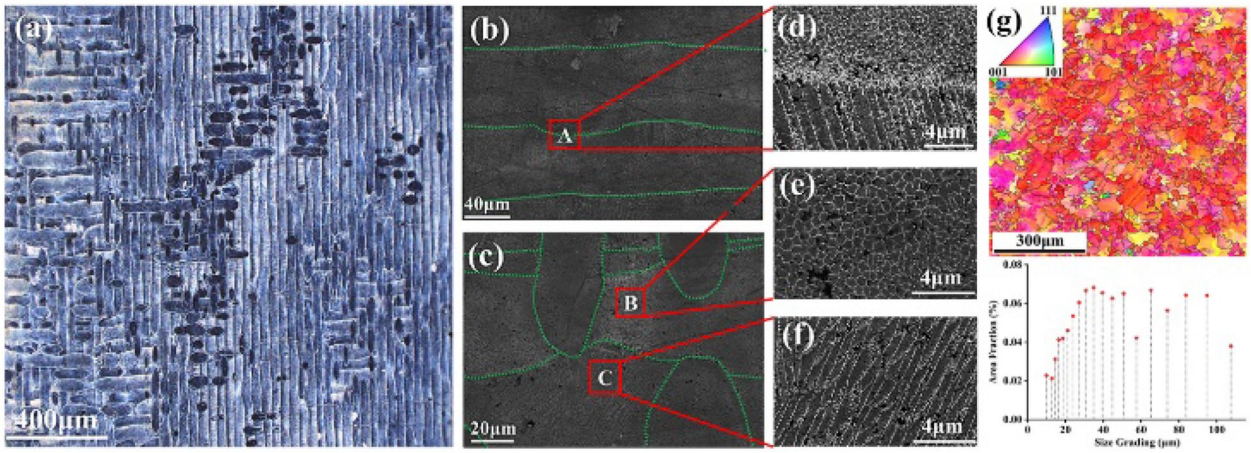

Figure 10 **a** The polished and etched *XY* surface of the SLMed sample; **b** Remelting area of the adjacent molten path; **c** Orthogonal laser scanning paths; **d** Region A; **e** Region B; **f** Region C; **g** Orientation map and size grading of the *XY* surface

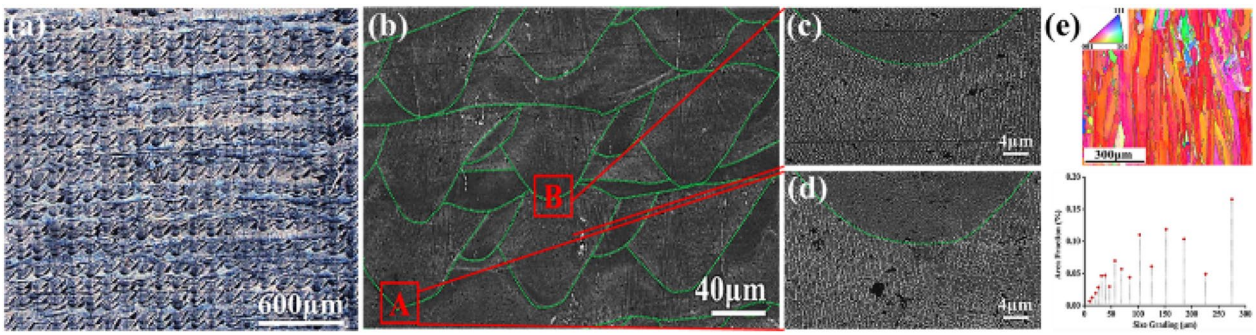

Figure 11 **a** The polished and etched *YZ* surface of the SLMed sample; **b** Cross-sectional view of molten pools; **c** Region B; **d** Region A; **e** Orientation map and size grading of the *YZ* surface

3.3 Effect of Processing Strategy

During the SLM process, solidification-related anisotropy could be observed in Figures 10, 11. The claddings on the *XY* surface were parallel to each other and perpendicular to the building direction as illustrated in Figure 10(a). Region A in Figure 10(b) is the remelting boundary of adjacent claddings, and Regions B and C in Figure 10(c) are the interior portion of the claddings. Figure 10d–f are enlarged images of Regions A, B and C in Figure 10(b) and (c). It can be seen that the microstructures of the *XY* surface are mainly composed of a small quantity of elongated columnar crystals and a great number of uniform cell crystals. Similar microstructures have been observed in Figure 11(c) and (d). Figure 11(c) and d are enlarged images of Regions A and B in Figure 11(b). The average grain size on the *XY* surface was about 46 μm as illustrated in Figure 10(g), much smaller than the centimeter-sized grains of the as-cast Inconel 738LC alloy [26]. The *YZ* surface showed "fish-scales" solidification morphology, as shown in Figure 10, which is consistent with that in Figure 3. Its width was approximately equal to the laser spot diameter of 90 μm, so the solidification morphology was determined by the scanning strategies and parameters. The *YZ* surface morphology exhibited a columnar structure that was parallel to the building direction with a length-width ratio of 10:1, as observed in Figure 10(e). The grain size was millimeter-sized lengthwise along the long axis and much smaller than that of the as-cast Inconel 738LC sample [26].

During the HSM process, there were three types of crystal structural changes in the machined surface due to machining-induced increases in temperature, strain, and strain rate, which could alter the surface integrity of the machined workpiece. From the surface to the bulk, the machining-affected layer was composed of a white layer, dark layer, and plastic deformation layer, up to dozens of microns in depth as illustrated in Figure 12. After being etched, the machining-affected layer with no

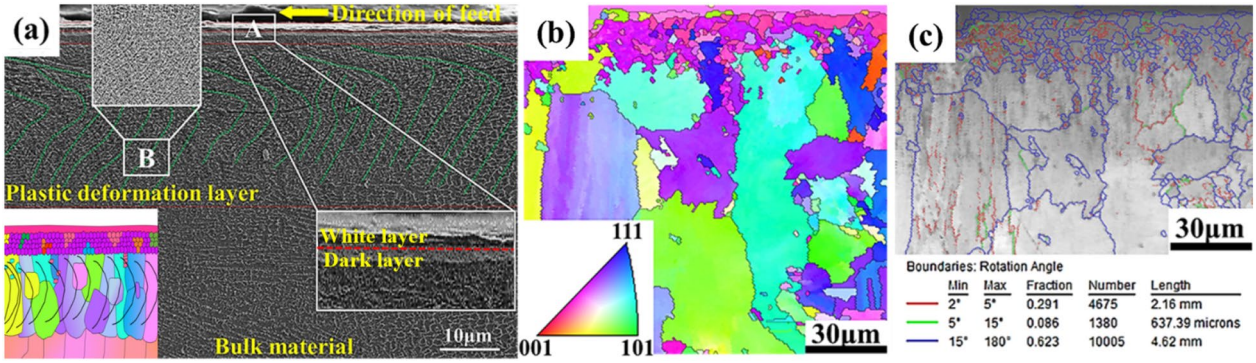

Figure 12 **a** Metamorphic layer of machined surface; **b** Orientation map; **c** Grain boundary rotation angles

characteristic morphology but a light color is referred to as the white layer [27], which is the outermost layer of the machined surface. The white layer has two properties, i.e., much harder and more brittle than the bulk and with severe grain refinement. The black transition zone below the white layer was defined as the dark layer. The grain orientation and boundary rotation angles changed dramatically beneath the white layer, as shown in Figure 12(b) and (c), the dark layer was a microcrystalline layer (Region A) whose thickness was a few microns. The plastic deformation layer (Region B) was below the dark layer, whose thickness was in dozens of microns. There was a boundary between the dark layer and the plastic deformation layer. The grain size of the dark layer was approximately a few microns [28, 29], far smaller than that of the bulk material. As illustrated in Region B of Figure 12(a), the plastic deformation layer was formed along the HSM feed direction like seagrasses. The grain orientation and boundary rotation angle of the plastic deformation layer are described in Figure 12(b) and (c). The boundary between the plastic deformation and the bulk layer is a fluctuating curve. The machining-affected layer widely exists in different kinds of machining processes, such as turning, milling, grinding, and electrical discharge machining [30, 31].

3.4 Surface Mechanical Properties

Remarkable anisotropy in hardness was obtained in the SLMed samples, as seen in Figure 13. Hardness is an important property for evaluating the surface strength and elastoplastic deformation resistance. Hardness of the SLMed and SLMed/HSMed samples was measured on different surfaces and compared with that of the as-cast sample [32]. The SLMed samples had a minimum hardness of 415.2 HV on the YZ surface and a maximum hardness of 452.8 HV on the XY surface. The SLMed/HSMed samples had a minimum hardness of 540.8 HV on the YZ surface and a maximum hardness of 587.6 HV on the XY surface. Their work-hardening index was about 130% compared to the SLMed samples and was 154.6% compared to the as-cast samples [26]. The SLMed/HSMed samples showed an anisotropic property on hardness.

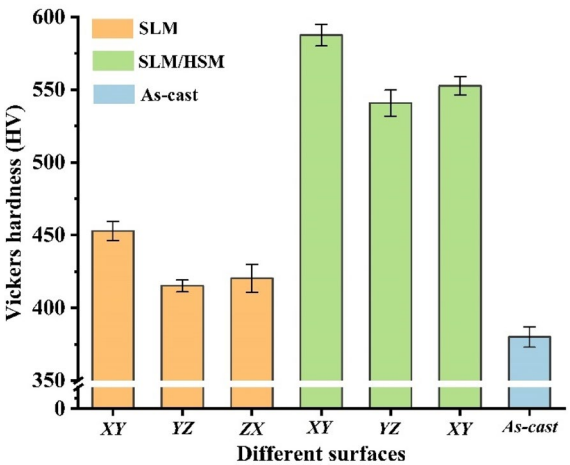

Figure 13 Hardness of the In738LC samples made by different processes

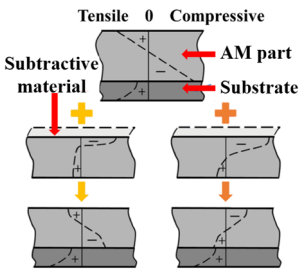

Figure 14 Diagrammatic illustration of residual stress coupling

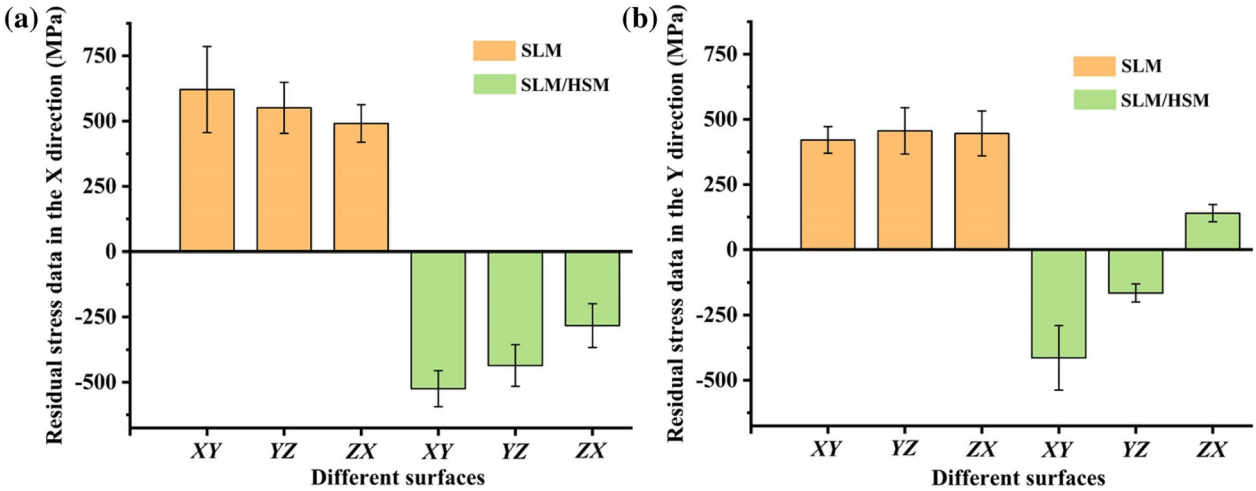

Figure 15 Residual stress of SLMed and SLMed/HSMed samples: **a** Residual stress in the *X* direction; **b** Residual stress in the *Y* direction

As illustrated in Figures 14 and 15, the residual stress states of the SLMed and SLMed/HSMed samples were significantly different. For the SLMed samples, the residual stresses on different surfaces were all tensile with a maximum of 786 MPa on the *XY* surface and a minimum of 107 MPa on the *ZX* surface. Residual stress in the SLM samples was tensile, which is pernicious to the fatigue life of a part [33]. The part failure location is prone to starting from the surface, especially in conditions of complex stress loads, high temperature and other extreme environments [34, 35], bringing in a beneficial residual compressive stress field which is an important strengthening mechanism to improve fatigue resistance and wear resistance of the part. For the SLMed/HSMed samples, the residual stress on different surfaces contains a maximum compressive stress of 594 MPa on the *XY* surface and a minimum compressive stress of 130 MPa on the *YZ* surface. During the HSM process, the surface residual stress was redistributed. Therefore, the surface residual stresses of SLMed/HSMed samples were determined by the coupling of the tensile stress generated in the SLM process and the compressive stress generated in the HSM process, as explained in Figure 14.

When the compressive stress generated in HSM was not large enough to suppress the tensile residual stress generated in the SLM process, the total residual stress was still in tensile condition. When the compressive stress generated in the HSM process was large enough to suppress the tensile residual stress generated in the SLM process, the total residual stress was compressive, as found in Figure 15.

4 Discussion

4.1 Formation Mechanisms of Machining Metamorphic Layer

As presented in Figures 10 and 11, the surface microstructure of the SLMed Inconel 738LC samples was composed of elongated dendritic structure without secondary dendrite arms and irregular hexagonal cellular crystals with a three-dimensional crystalline structure similar to the hexagonal prisms, as found in Figure 16(a). Such metastable state microstructure was widespread in the SLMed materials. The high cooling rate and directional heat conduction in the SLM process are believed to play a significant role in the microstructure formation [36] with its preferable growth direction determined by

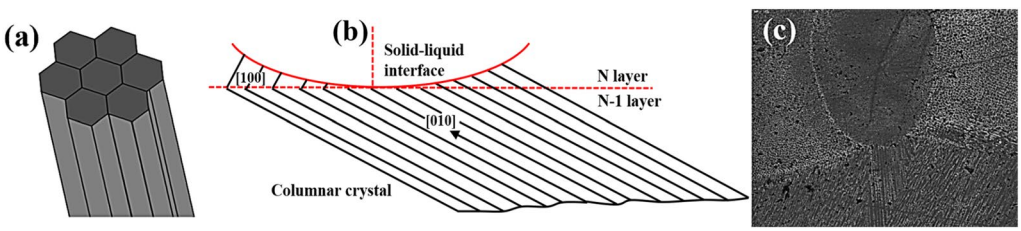

Figure 16 **a** Illustrations of the metastable three-dimensional columnar microstructure; **b** Schematic diagram and **c** SEM photograph of the crystal growth direction between two adjacent layers

the fastest growing crystallographic orientation and the local temperature gradient field of the molten pool front. Inconel 738LC has an FCC structure with more intricate elements and phases in the [100] direction for its fastest growing crystallographic orientation that is closest to the temperature gradient direction. The temperature gradient (G) and the crystal growth rate (R) play a decisive role in the microstructure formation. A flat solidification morphology is obtained at an extremely high G/R ratio; columnar crystals at a low G/R ratio and cellular crystals are formed at an intermediate G/R ratio [37]. Furthermore, the crystal growth starts from the heat-affected zone of the substrate layer along or perpendicular to the original direction, as schematically shown in Figure 16(b). The crystallographic orientation of the previous layer significantly affects the microstructure of the next layer. Since the crystallographic orientation of the substrate is usually random, the epitaxial growth direction of the microstructure of the SLMed Inconel 738LC sample is also random over the <100> crystal plane. Moreover, the Benard-Marangoni instability phenomenon usually occurs at the solid/liquid interface of the molten pool, which may result in asymmetric microstructures, as imaged in Figure 16(c). In summary, the microstructure of a SLMed part can be regulated by designing special process parameters to control the direction of the temperature gradient. Through microstructure manipulation, a SLMed part with desirable mechanical properties can be obtained.

A mixed microstructure of slender and finer grains can be observed at the interface of the SLM/HSM manufactured parts. The high cooling rate and direction of heat conduction in the SLM process are considered the main mechanisms dominating the microstructure formation. The growth direction of the microstructure is determined by the crystallographic orientation of the fastest growth and the local temperature gradient field at the melting surface. The relationship between the growth crystallographic orientation of the previous layer and the direction of the temperature gradient field in the next layer can significantly affect the formation of microstructure. Since the crystallographic orientation of the surface metamorphic layer formed in the HSM process is usually random, the epitaxial growth direction of the microstructure in the next layer during the SLM process is randomly distributed over the interface.

Figure 17 shows schematics of the microstructure of (a) the machined surface; and (b) the interface of a SLMed/HSMed part. The formation of the machining metamorphic layer during the HSM process has been a scientific issue of great significance and is to be explored. According to the previous result, the machining-affected layer is composed of a white layer, a dark layer, and a plastic deformation layer from the surface to the bulk. According to the previous research, the white layer formed due to grain nanocrystallization induced by phase transition [38–43]. The white layer can not only be formed under high temperature and high strain conditions, but also under low temperature and low strain conditions, as described in Figure 18(a). The conventional "thermal-plastic deformation mechanism" cannot clearly explain the formation mechanism of the white layer. Therefore, the formation of the white layer can be described as the phase transformation and grain refinement of the surface layer caused by the “thermal-mechanical coupling effect” of temperature, strain, and strain rate of the machined surface as illustrated in Figure 18(c). Meanwhile, this study found that the relationship between temperature and strain rate was inversely proportional to the overall trend as shown in Figure 18(b). Zhang et al. [44] also observed that the thickness of the white layer decreased with an increase in cutting speed. Therefore, the formation of the white layer cannot be fully explained by the "thermal-strain rate mechanism" alone [45–47]. The critical temperature for the formation of a white layer decreases with an increase in strain but a decrease in strain rate [48]. During the HSM process, the high cutting speed results in a decrease in both temperature and

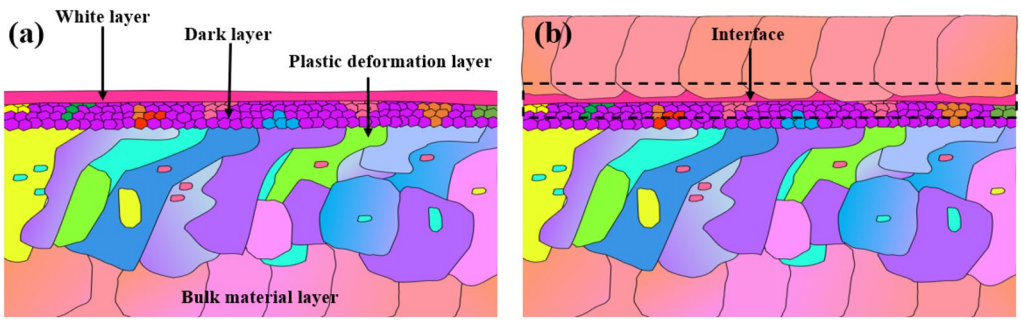

Figure 17 Schematics of **a** machined surface and **b** interface of SLMed/HSMed part

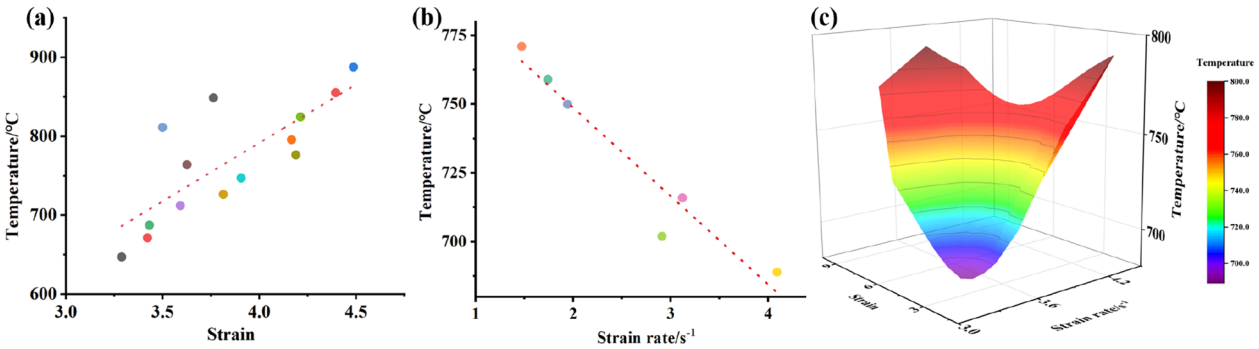

Figure 18 Formation conditions of white layer: **a** temperature and strain; **b** temperature and strain rate; **c** temperature, strain and strain rate [38–43]

strain but an increase in strain rate, which inhibits the formation of the white layer, the thickness of the white layer decreased with an increase in cutting speed.

The "thermal-mechanical coupling effect" also has different roles in the grain refinement and deformation of the dark layer and plastic deformation layer [49, 50]. Dynamic recovery and recrystallization induced by high temperature and plastic deformation are the dominant mechanisms for the formation of a dark layer during HSM, which has been reported elsewhere [29, 44]. The dark layer is essentially a kind of microstructure induced by high temperature tempering. Under the action of the "thermal-mechanical coupling effect", the grain boundary is re-formed due to plastic deformation, leading to grain refinement in the dark layer. The plastic deformation not only provides the driving force for dynamic recrystallization but also affects the grain refinement process of the dark layer [51, 52]. It has been revealed that high temperature, large strain, and low strain rate are favorable to the dynamic recrystallization of the high temperature tempered microstructure [53, 54]. In the HSM process, the temperature and strain of the dark layer decrease, and the strain rate increases with an increase in cutting speed [55, 56]. During the HSM process, the dynamic recrystallization of the dark layer is inhibited, dark layer grain is refined. Under the dark layer, crystal grains of the plastic deformation layer slip and the dislocations nucleate and evolve, leading to grain elongation and refinement [57]. In addition, a higher cutting speed increases the shear strain of workpieces on the one hand and decreases the depth of plastic deformation in the workpiece on the other hand [58]. Therefore, SLM/HSM hybrid manufacturing is an effective method to obtain a better surface with thinner machining metamorphic layer [55].

4.2 Mechanical Properties of the Machining Metamorphic Layer

The residual stress evolution of the machining metamorphic layer during the SLM/HSM process is another scientific issue worth investigating. Residual stress in a SLMed/HSMed sample is related to the stress evolution from white layer, dark layer, plastic deformation layer, and bulk material layer. As schematically shown in Figure 19, the stress evolution in the melting and solidification processes shows significant variations in the SLM process. In the melting process, metal powders melt from solid phase to liquid phase. The volume of the melt pool tends to expand in the solidification process. The surrounding solid material restricts its expansion. As a result, compressive stress is generated at the melt pool boundary (the heat affected zone), as sketched in Figure 19(a). The melt pool shows no stress in its interior but the largest compressive stress at the boundary [59]. The stress evolution in multilayer melting of cyclic thermal loading can be divided into three stages: the original stress stage, the stress relief stage, and the stress building stage [60]. In the solidification process, the molten pool changes from liquid to solid with a shrunk volume. The compressive stress changes into tensile at the melt pool boundary, as depicted in Figure 19b. A higher residual tensile stress is induced in the solidified pool interior

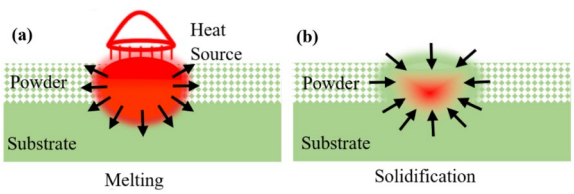

Figure 19 Schematics of residual stress evolution of **a** melting process and **b** solidification process

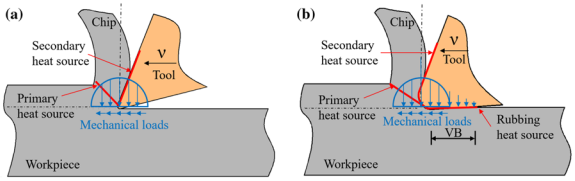

Figure 20 Schematics of cutting process of **a** new and **b** worn cutting tool

at a high solidification rate because of the restriction to shrinkage offered by the neighboring material [59].

According to the previous experimental results, the surface residual stress of the SLMed Inconel 738LC was redistributed during the HSM process. As schematically described in Figure 20a, the tool rake face pushes the chip, and a plastic deformation layer is formed on the machined surface [61]. Compressive stress can be formed by the extrusion of the tool and approaches a stable value with an increase in depth from a machined surface [62]. In the meantime, the frictional force is generated between the flank face and the machined surface, as schematically described in Figure 20(b), which may lead to the formation of the white layer and dark layer [63]. During the milling process, the material within the machining zone expands with temperature rise and shrinks at the cooling stage [64]. The final state of residual stress is a result of the combined effect of the thermal and mechanical stresses. In the white layer and dark layer, not only the compressive residual stress but also the tensile residual stress may be generated, which can result in a change of residual stress from compressive to tensile as the tool wear progresses [65–67]. In addition, residual stress is also related to cutting speed. It can change from compressive to tensile at an increased cutting speed [44, 68]. Selecting the appropriate machining parameters is an effective way to decrease cutting force and suppress machining heat so as to form beneficial residual compressive stress in a machined surface. However, there is a lack of understanding of the relationship between residual stress and thermal/mechanical loads, which needs further investigation in future work.

5 Conclusions

In this study, surface integrity in high-speed milling of SLM-built Inconel 738LC parts is investigated in regard to the powder morphology, surface quality, microstructure alteration, and mechanical property. A summary is as follows.

(1) A remarkable anisotropy of the surface solidification morphology and microstructure is found in the building direction.
(2) SLM/HSM hybrid manufacturing can be an effective method for obtaining better surface quality with thinner machining metamorphic layer by increasing cutting speed.
(3) Selecting high-speed machining is an effective way to form beneficial residual compressive stress in the machined surface during the SLM/HSM hybrid manufacturing process.

Acknowledgements
Not applicable.

Author contributions
BZ was in charge of the whole trial; GR wrote the manuscript; SG assisted with sampling and laboratory analyses. All authors read and approved the final manuscript.

Authors' Information
Guanhui Ren, born in 1993, is currently an engineer in *Shenzhen Xinjinquan Precision Techonology Co., Ltd., Shenzhen, China,* and an on-the-job graduate student in *Shandong University*, *China*.
Sai Guo, born in 1993, now is a Ph.D. candidate in *Southern University of Science and Technology, China*. His major research interest is high-speed grinding.
Bi Zhang, born in 1957, is currently a chair professor in *Southern University of Science and Technology, China*. His research interests include precision machining and additive/subtractive hybrid manufacturing.

Funding
Supported by Shenzhen Municipal Science and Technology Innovation Commission Projects (Grant Nos. Y01336107, JCYJ20180504165824643, GJHZ20180411143506667, JC YJ20170817111811303 and KQTD20190929172505711).

Competing interests
The authors declare no competing financial interests.

Received: 10 October 2021 Revised: 11 October 2022 Accepted: 18 December 2022
Published online: 16 January 2023

References

[1] O Ojo, N Richards, M Chaturvedi. Liquid film migration of constitutionally liquated γ in weld heat affected zone (HAZ) of Inconel 738LC superalloy. *Scripta Materialia*, 2004, 51(2): 141-146.
[2] J Ma, F Wang, Z Jia, et al. Machining parameter optimization in high-speed milling for Inconel 718 curved surface. *Materials and Manufacturing Processes*, 2016, 31(13): 1692-1699.
[3] I Gibson, D Rosen, B Stucker. Additive manufacturing technologies. New York: Springer US, 2015.
[4] L Zhu, S Wang, H Pan, et al. Research on remanufacturing strategy for 45 steel gear using H13 steel powder based on laser cladding technology. *Journal of Manufacturing Processes*, 2020, 49: 344-354.
[5] L Zhu, P Xue, Q Lan, et al. Recent research and development status of laser cladding: A review. *Optics & Laser Technology*, 2021, 138: 106915.
[6] L Zhu, Z Yang, B Xin, et al. Microstructure and mechanical properties of parts formed by ultrasonic vibration-assisted laser cladding of Inconel 718. *Surface and Coatings Technology*, 2021, 410: 126964.
[7] W Du, Q Bai, B Zhang. A novel method for additive/subtractive hybrid manufacturing of metallic parts. *Procedia Manufacturing*, 2016, 5: 1018-30.
[8] C Liu, D Yan, J Tan, et al. Development and experimental validation of a hybrid selective laser melting and CNC milling system. *Additive Manufacturing*, 2020: 101550.
[9] SODICK. Shaping new ideas with accumulated technical excellence. OPM250L/OPM350L Catalogue. https://www.sodick.co.jp/product/tool/

metal_3d_printer/special/index_en.html. 2020 (Accessed 01 September 2020)
[10] D Wang, Y Zhou, J Shen, et al. Selective laser melting under the reactive atmosphere: a convenient and efficient approach to fabricate ultrahigh strength commercially pure titanium without sacrificing ductility. *Materials Science & Engineering A*, 2019, 762: 138078.
[11] W Du, Q Bai, B Zhang. Machining characteristics of 18Ni-300 steel in additive/subtractive hybrid manufacturing. *International Journal of Advanced Manufacturing Technology*, 2018, 95(5-8): 2509-19.
[12] D Bhaduri, P Penchev, K Essa, et al. Evaluation of surface/interface quality, microstructure and mechanical properties of hybrid additive-subtractive aluminium parts. *CIRP Annals*, 2019, 68(1): 237-40.
[13] Q Bai, B Wu, X Qiu, et al. Experimental study on additive/subtractive hybrid manufacturing of 6511 steel: Process optimization and machining characteristics. *International Journal of Advanced Manufacturing Technology*, 2020, 108(5): 1389-98.
[14] SODICK. High power laser & high speed milling. OPM250L/OPM350L Catalogue https://www.sodick.co.jp/product/tool/metal_3d_printer/special/index_en.html. 2020 (Accessed 01 January 2020)
[15] Q Yang, Y Hu, Y Ding, et al. Properties and formability of IN 738 alloy powder for selective laser melting. *Laser & Optoelectronics Progress*, 2019, 10: 194-201.
[16] D Gu, M Xia, D Dai. On the role of powder flow behavior in fluid thermodynamics and laser processability of Ni-based composites by selective laser melting. *International Journal of Machine Tools and Manufacture*, 2019, 137: 67-78.
[17] Y Cheng, H, Guan L Bo, et al. Characteristics and applications of metal powders for 3D printing. *Materials Review*, 2017, 31: 98-101.
[18] S Yan, A Zhang, S Liang, et al. Measurement of laser light absorptivity of commonly used metals in laser additive manufacturing technique. *Aeronautical Manufacturing Technology*, 2017(17): 97-100.
[19] R Peng, L Lan, L Yong, et al. Research progress in coaxial powder feeding nozzles. *Laser & Optoelectronics Progress*, 2017, 54(8): 080004.
[20] M Tan, Y Shin. Investigation of vapor plume and molten pool in pulsed and continuous keyhole welding based on a three-dimensional dynamic model. *Proceedings of the Aeromat 24 Conference and Exposition American Society for Metals*, Bellevue, Washington, USA, 2013.
[21] J Liu, P Zeng, Z Rao, et al. Transport phenomena and keyhole evolution process in laser welding of stainless steel. *Journal of Central South University*, 2019, 26(8): 2088-2099.
[22] J Yang, J Han, H Yu, et al. Role of molten pool mode on formability, microstructure and mechanical properties of selective laser melted Ti-6Al-4V alloy. *Materials & Design*, 2016, 110: 558-570.
[23] B Liu, G Fang, L Lei. An analytical model for rapid predicting molten pool geometry of selective laser melting (SLM). *Applied Mathematical Modelling*, 2021, 92: 505-524.
[24] S Sing, W Yeong, F Wiria, et al. Direct selective laser sintering and melting of ceramics: A review. *Rapid Prototyping Journal*, 2017, 23(3): 611-623.
[25] A Sutton, C Kriewall, M Leu, et al. Powder characterisation techniques and effects of powder characteristics on part properties in powder-bed fusion processes. *Virtual and Physical Prototyping*, 2017, 12(1): 3-29.
[26] K Kunze, T Etter, J Grässlin, et al. Texture, anisotropy in microstructure and mechanical properties of IN738LC alloy processed by selective laser melting (SLM). *Materials Science and Engineering: A*, 2015, 620: 213-222.
[27] S Bosheh, P Mativenga. White layer formation in hard turning of H13 tool steel at high cutting speeds using CBN tooling. *International Journal of Machine Tools and Manufacture*, 2006, 46(2): 225-233.
[28] J Zhou, V Bushlya, R Peng, et al. Effects of tool wear on subsurface deformation of nickel-based superalloy. *Procedia Engineering*, 2011, 19: 407-413.
[29] X Xu, J Zhang, H Liu, et al. Grain refinement mechanism under high strain-rate deformation in machined surface during high speed machining Ti6Al4V. *Materials Science and Engineering: A*, 2019, 752: 167-179.
[30] A Attanasio, D Umbrello, C Cappellini, et al. Tool wear effects on white and dark layer formation in hard turning of AISI 52100 steel. *Wear*, 2012, 286-287: 98-107.
[31] A Vyas, M Shaw. The significance of the white layer in a hard turned steel chip. *Machining Science and Technology*, 2000, 4(1): 169-175.
[32] P Wang, P Jariyasakuntham, S Polsilapa, et al. Effects of Al additions and reheat treatments on microstructures of modified nickel-based superalloy, grade Inconel 738, by vacuum arc melting process. *Advanced Materials Research*, 2014, 1025-1026: 395-402.
[33] R Moat, A Pinkerton, L Li, et al. Residual stresses in laser direct metal deposited Waspaloy. *Materials Science and Engineering: A*, 2011, 528(6): 2288-2298.
[34] X Liang, Z Liu, B Wang. State-of-the-art of surface integrity induced by tool wear effects in machining process of titanium and nickel alloys: A review. *Measurement*, 2019, 132: 150-181.
[35] D Novovic, R Dewes, D Aspinwall, et al. The effect of machined topography and integrity on fatigue life. *International Journal of Machine Tools and Manufacture*, 2004, 44(2): 125-134.
[36] D Kong, C Dong, S Wei, et al. About metastable cellular structure in additively manufactured austenitic stainless steels. *Additive Manufacturing*, 2021, 38: 101804.
[37] S Kou. Welding metallurgy. 2nd edition. New York: John Wiley, 2003.
[38] Z Chen, M Colliander, G Sundell, et al. Nano-scale characterization of white layer in broached Inconel 718. *Materials Science and Engineering: A*, 2017, 684: 373-384.
[39] M Brown, P Crawforth, R M'Saoubi, et al. Quantitative characterization of machining-induced white layers in Ti-6Al-4V. *Materials Science and Engineering: A*, 2019, 764: 138220.
[40] S Buchkremer, F Klocke, B Döbbeler, et al. Thermodynamics-based interpretation of white layer formation in metal cutting. *Procedia CIRP*, 2017, 58: 370-374.
[41] L Li, D Lai, Q Ji, et al. Influence of tool characteristics on white layer produced by cutting hardened steel and prediction of white layer thickness. *The International Journal of Advanced Manufacturing Technology*, 2021, 113(3): 1215-1228.
[42] R Hossain, F Pahlevani, E Witteveen, et al. Hybrid structure of white layer in high carbon steel – Formation mechanism and its properties. *Scientific Reports*, 2017, 7(1): 13288.
[43] Z Liu, S Lv. Thermo-mechanical coupling mechanisms for white layer formation on machined surface of powder metallurgical nickel-based superalloy. *Journal of Mechanical Engineering*, 2014, 50(17): 186-93.
[44] F Zhang, C Duan, W Sun, et al. Effects of cutting conditions on the microstructure and residual stress of white and dark layers in cutting hardened steel. *Journal of Materials Processing Technology*, 2019, 266: 599-611.
[45] R Bulpett, T Eyre, B Ralph. The characterization of white layers formed on digger teeth. *Wear*, 1993, 162-164: 1059-1065.
[46] C Duan, F Zhang, W Sun, et al. White layer formation mechanism in dry turning hardened steel. *Journal of Advanced Mechanical Design, Systems, and Manufacturing*, 2018, 12(2): JAMDSM0044.
[47] J Du, S Lv. Deformation-phase transformation coupling mechanism of white layer formation in high speed machining of FGH95 Ni-based superalloy. *Applied Surface Science*, 2014, 292: 197-203.
[48] S Han, S Melkote, M Haluska, et al. White layer formation due to phase transformation in orthogonal machining of AISI 1045 annealed steel. *Materials Science and Engineering: A*, 2008, 488(1-2): 195-204.
[49] J Zhou, V Bushlya, J Stahl. An investigation of surface damage in the high speed turning of Inconel 718 with use of whisker reinforced ceramic tools. *Journal of Materials Processing Technology*, 2012, 212(2): 372-384.
[50] X Liang, Z Liu. Experimental investigations on effects of tool flank wear on surface integrity during orthogonal dry cutting of Ti-6Al-4V. *International Journal of Advanced Manufacturing Technology*, 2017, 93(5): 1617-1626.
[51] T Sakai, A Belyakov, R Kaibyshev, et al. Dynamic and post-dynamic recrystallization under hot, cold and severe plastic deformation conditions. *Progress in Materials Science*, 2014, 60: 130-207.
[52] C Ghosh, V Basabe, J Jonas. Determination of the critical strains for the initiation of dynamic transformation and dynamic recrystallization in four steels of increasing carbon contents. *Steel Research International*, 2013, 84(5): 490-494.
[53] S Mandal, M Jayalakshmi, A Bhaduri, et al. Effect of strain rate on the dynamic recrystallization behavior in a nitrogen-enhanced 316L(N). *Metallurgical and Materials Transactions A*, 2014, 45(12): 5645-5656.
[54] D Dong, Y Liu, L Wang, et al. Effect of strain rate on dynamic deformation behavior of DP780 steel. *Acta Metall Sin*, 2013, 49(2): 159-166.
[55] B Zhang, J Yin. The "skin effect" of subsurface damage distribution in materials subjected to high-speed machining. *International Journal of Extreme Manufacturing*, 2019, 1(1): 012007.

[56] X Yang, B Zhang. Material embrittlement in high strain-rate loading. *International Journal of Extreme Manufacturing*, 2019, 1(2): 022003.
[57] M Yaghoobi, G Voyiadjis. Microstructural investigation of the hardening mechanism in FCC crystals during high rate deformations. *Computational Materials Science*, 2017, 138: 10-15.
[58] D Jin, Z Liu. Damage of the machined surface and subsurface in orthogonal milling of FGH95 superalloy. *The International Journal of Advanced Manufacturing Technology*, 2013, 68(5): 1573-1581.
[59] R Sharma, S Saxena, A Kumar. Thermal stress analysis in selective laser melting of Ti6Al4V powder layer. *Application of Lasers in Manufacturing*, 2019: 95-110.
[60] Z Xiao, C Chen, H Zhu, et al. Study of residual stress in selective laser melting of Ti6Al4V. *Materials & Design*, 2020, 193: 108846.
[61] X Liang, Z Liu, B Wang, et al. Modeling of plastic deformation induced by thermo-mechanical stresses considering tool flank wear in high-speed machining Ti-6Al-4V. *International Journal of Mechanical Sciences*, 2018, 140: 1-12.
[62] F Jafarian. 3D modeling of recrystallized layer depth and residual stress in dry machining of nickel-based alloy. *Journal of the Brazilian Society of Mechanical Sciences and Engineering*, 2019, 41(4): 198.
[63] S Zhang, J Li, H Lv. Tool wear and formation mechanism of white layer when hard milling H13 steel under different cooling/lubrication conditions. *Advances in Mechanical Engineering*, 2014, 6: 949308.
[64] X Shen, D Zhang, C Yao, et al. Formation mechanism of surface metamorphic layer and influence rule on milling TC17 titanium alloy. *International Journal of Advanced Manufacturing Technology*, 2021, 112(7): 2259-2276.
[65] F Zhang, C Duan, M Wang, et al. White and dark layer formation mechanism in hard cutting of AISI52100 steel. *Journal of Manufacturing Processes*, 2018, 32: 878-887.
[66] Y Guo, A Warren, F Hashimoto. The basic relationships between residual stress, white layer, and fatigue life of hard turned and ground surfaces in rolling contact. *CIRP Journal of Manufacturing Science and Technology*, 2010, 2(2): 129-134.
[67] Y Guo, J Sahni. A comparative study of hard turned and cylindrically ground white layers. *International Journal of Machine Tools and Manufacture*, 2004, 44(2): 135-145.
[68] F Zhang. *Study on microstructure and wear resistance of the metamorphic layer of GCr 15 bearing steel in hard cutting*. Dalian: Dalian University of Technology, 2019.